Received: 26 May 2019 | Revised: 27 October 2019 | Accepted: 28 October 2019

DOI: 10.1002/joc.6385

RESEARCH ARTICLE

International Journal of Climatology RMetS

"Surface," "satellite" or "simulation": Mapping intra-urban microclimate variability in a desert city

Bin Zhou[1,4] | **Shai Kaplan**[1] | **Aviva Peeters**[2] | **Itai Kloog**[3] | **Evyatar Erell**[1,3]

[1]The Jacob Blaustein Institutes for Desert Research, Ben-Gurion University of the Negev, Sde Boqer Campus, Israel

[2]TerraVision Lab, Beersheba, Israel

[3]Department of Geography and Environmental Development, Ben-Gurion University of the Negev, Beer Sheva, Israel

[4]Potsdam Institute for Climate Impact Research (PIK), Member of the Leibniz Association, Potsdam, Germany

Correspondence
Bin Zhou, The Jacob Blaustein Institutes for Desert Research, Ben-Gurion University of the Negev, Sde Boqer Campus, 8499000, Israel.
Email: zhoub@post.bgu.ac.il

Funding information
Israel Ministry of Science, Technology and Space, Grant/Award Number: 63365; Jewish National Fund; Kreitman School for Advanced Graduate Studies of the Ben-Gurion University of the Negev and the PBC Fellowship Program; Jacob Blaustein Center for Scientific Cooperation

Abstract

Mapping spatial and temporal variability of urban microclimate is pivotal for an accurate estimation of the ever-increasing exposure of urbanized humanity to global warming. This particularly concerns cities in arid/semi-arid regions which cover two fifths of the global land area and are home to more than one third of the world's population. Focusing on the desert city of Be'er Sheva Israel, we investigate the spatial and temporal patterns of urban–rural and intra-urban temperature variability by means of satellite observation, vehicular traverse measurement, and computer simulation. Our study reveals a well-developed nocturnal canopy layer urban heat island in Be'er Sheva, particularly in the winter, but a weak diurnal cool island in the mid-morning. Near surface air temperature exhibits weak urban–rural and intra-urban differences during the daytime (<1°C), despite pronounced urban surface cool islands observed in satellite images. This phenomenon, also recorded in some other desert cities, is explained by the rapid increase in surface skin temperature of exposed desert soils (in the absence of vegetation or moisture) after sunrise, while urban surfaces are heated more slowly. The study highlights differences among the three methods used for describing urban temperature variability, each of which may have different applications in fields such as urban planning, climate change mitigation, and epidemiological research.

1 | INTRODUCTION

The world is becoming increasingly urbanized, with more than half of its population living in cities for the first time in history (UN, 2015). As one of the most evident anthropogenic modifications of the Earth's natural landscape, urbanization encompasses two principal concerns facing our era: population growth and climate change. The far-reaching consequences of urbanization on both climate and society are manifested in the urban heat island (UHI)—a phenomenon where urban areas experience a higher temperature relative to their rural surroundings, especially at night (Oke, 1987).

The causes for the UHI have been well studied (Oke, 1981, 1982) and documented globally (Arnfield, 2003). The spatial and temporal dynamics of the UHI have also been studied extensively and been shown to be subject to numerous factors, such as the overarching meteorological conditions, underlying land use, and land cover heterogeneity (Pielke, 2001; Weaver and Avissar, 2001; Lookingbill and Urban, 2003; Erell and Williamson, 2007; Georgescu *et al.*, 2012; Loridan and Grimmond, 2012), and 3D geometry (Kaplan *et al.*, 2016). These factors result in substantial intra-urban differences in climate, generating a need for a classification system of Local Climate Zones (LCZ) (Stewart

This is an open access article under the terms of the Creative Commons Attribution-NonCommercial License, which permits use, distribution and reproduction in any medium, provided the original work is properly cited and is not used for commercial purposes.
© 2019 The Authors. International Journal of Climatology published by John Wiley & Sons Ltd on behalf of the Royal Meteorological Society.

and Oke, 2012). However, microclimates may differ substantially even within LCZs, and methods of studying and documenting conditions within cities should be able to resolve these variations at appropriate spatial and temporal scales (Georgescu *et al*., 2015). The three most common methodologies—in-situ measurements (transects or point measurements), remote sensing, and model simulations—are summarized in Table 1 and described in brief below.

1.1 | Field measurements

In-situ measurements may provide accurate data but have several limitations. Point measurements can provide continuous data but are limited by the number of locations monitored simultaneously, especially if long-term data are required, for example, as the basis for generating Typical Meteorological Years (TMYs) for building design. Regression and geo-statistical models can interpolate data to create a continuous spatial map (Szymanowski and Kryza, 2012; Ivajnšič *et al*., 2014; Oyler *et al*., 2015), yet they are site-specific and highly dependent on the interpolation parameters/techniques applied. Mobile transects provide high accuracy data with the additional advantage of continuity in the spatial domain. However, like point measurements, they represent only the time of measurements and are highly influenced by the methodological design (e.g., route selection, movement of measurement platform), and platforms where measuring instruments are mounted (e.g., vehicles, bicycles). In addition, in-situ methodologies are expensive, labour intensive, time-consuming, and thus not always feasible.

1.2 | Thermal remote sensing

Remote sensing measures surface skin temperature, also known as land surface temperature (LST). LST refers to the ground radiometric temperature seen from above and is a measure of the energy emitted and reflected from the surface. Hence, LST represents the effects of surface radiative properties, thermodynamics, and near-surface atmosphere processes (Mirzaei and Haghighat, 2010). This energy in turn affects air temperature (T_a) along with other variables such as wind, moisture, and turbulent mixing. Thermal remote sensing is capable of quantifying and monitoring surface skin temperature over large areas at relatively high spatial resolution. Depending on the satellite sensor, the spatial resolution of thermal remote sensing varies from tens of meters (e.g., from Landsat series) to several kilometres (e.g., for geostationary satellites). However, the thermal remote sensing is limited to clear-sky conditions. Subject to orbit and revisit period, most satellites cannot provide a continuous record at short time intervals (e.g., hourly) and thus are insufficient to monitor and model the nocturnal UHI (Yang *et al*., 2013). Nevertheless, several studies have demonstrated good correlation between radiant temperature and canopy level air temperature (Kloog *et al*., 2012, 2017; Pelta *et al*., 2016; Rosenfeld *et al*., 2017), and the technique has been applied in research on the effect of heatwaves on mortality (Laaidi *et al*., 2011). However, the complex linkage between surface- and air-temperatures hampers our endeavours in estimating one temperature from the other. In particular, the 3D nature

TABLE 1 Methods of obtaining urban temperature

	In-situ measurement (traverse)	Satellite remote sensing	Simulation
Spatial resolution (scale)	Limited number of points representative of micro-scale (1–10^4 m^2) ambiance	Sensor-dependent, from micro- to local-scale (10^5–10^7 m^2)	Depends on model settings
Temporal resolution	Single data point for each stop on traverse	Continuous (geostationary) or periodic (polar-orbiting)	Model-dependent
Level	Screen level (air temperature at approximately 2 m height)	Skin level (surface skin temperature)	No constraint
Weather conditions	All weather	Clear sky only	All weather
Surface features	Accessible (by car, bicycle or foot)	Surfaces exposed to the sky	Depends on model
Applications	Model validation	"Backcasting," epidemiology	Scenario testing, prognostic

of cities limits the sensor's ability to view all surfaces. In dense high-rise cities (e.g., in New York City) LST may represent the surface temperature of rooftops rather than the actual street canyon. In addition, a bird's-eye view is limited in the view angle, that is, even if it sees the street level, it cannot measure the energy emitted from vertical surfaces such as a building wall (Voogt and Oke, 2003).

1.3 | Simulation

In a simulation approach, models are used to represent urban details and the governing processes of energy balance and/or fluid dynamics. Based primarily on governing equations, spatial, and temporal resolution, models in simulating urban climate can be classified into three groups (Mirzaei and Haghighat, 2010): (a) Urban Canopy Models (e.g., the Town Energy Balance model [Masson, 2000]); (b) micro-scale Computational Fluid Dynamics (CFD) models (e.g., ENVI-met [Bruse and Fleer, 1998]); and (c) meso-scale CFD models (e.g., the Weather Research and Forecasting [WRF] model coupled with an explicit urban canopy model [Chen *et al*., 2011]).

The simulation approach allows researchers to predict the intra-urban temperature variability under different scenarios of climate and urban morphology. However, models often require very detailed input and substantial computational resources. They are limited in either their spatial or temporal extent and require great expertise to implement. Most models generate output ill-suited to planners needs and are thus applied principally in academic research rather than in urban planning practice (Mills *et al*., 2010).

In most studies only one of these three methods is applied. This necessarily leads to limitations in addressing the complexity that is inherent in urban microclimate. Such studies are of course still valuable, if their limitations are recognized explicitly and interpretation of results is constrained to the appropriate spatial and temporal framework. However, this is not always the case. For example, tools that were developed for detailed micro-scale modelling of plant-atmosphere interactions in limited spatial confines in the built environment, such as ENVI-met, cannot generate TMY files required for building energy modelling. Conversely, methods currently employed for building energy modelling cannot yet account for the full complexity of urban vegetation. Yet both approaches are routinely applied (separately) in studies that seek to establish the effects of vegetation on building energy demand, and are used to generate recommendations for mitigating the UHI—despite their inherent limitations. Different methods may also lead to different results. For example, Sheng *et al*. (2017) acknowledged explicitly that although LST drives near surface air temperature, they displayed opposite seasonal trends, so that LST-based UHI is greater in summer than in winter, the air temperature UHI is greater in winter. Hartz *et al*. (2006) found that the use of thermal remote sensing to derive night time air temperature could describe surface heterogeneity well, but that daytime ranking of the same neighbourhoods by temperature based on thermal imaging was inconsistent with ground measurements.

Implementation of all of the aforementioned methods may also suffer from inadvertent bias, because they have mostly been carried out in temperate climates, despite the fact that arid or semi-arid regions cover over 40% of the global land and are home to over one third of the world's population (Pearlmutter *et al*., 2007; Koohafkan and Stewart, 2008). The assumption, often left unstated, is almost always that cities are drier than their rural surroundings, and that LST in the city is higher. Yet as Oke *et al*. (1998) demonstrated, this may not be the case. So while there has been an increase in studies of urban microclimate in tropical and wet subtropical areas (see review in Roth, 2007) the only desert city where microclimate has been studied extensively is Phoenix, Arizona (e.g., Baker *et al*., 2002; Brazel and Hedquist, 2006; Guhathakurta and Gober, 2010; Svoma and Brazel, 2010; Middel *et al*., 2012, 2014). This is despite the fact that several studies have found important differences between desert cities and temperate ones (Brazel *et al*., 2000; Lazzarini *et al*., 2015).

The objectives of this study are thus twofold: (a) to compare and contrast the three different methods for evaluating the thermal dynamics/behaviour of a complex urban environment, and (b) to add to the relatively small sample of studies on the microclimate of desert cities. Taking the city of Be'er Sheva, Israel, as a case study, we investigate the spatio-temporal pattern of intra-urban temperature variations by means of mobile traverse measurements, computer simulation of near-surface air temperature, and LST from satellite remote sensing. The juxtaposition of results obtained by these methods illustrates their relative advantages and drawbacks.

2 | DATA AND METHODS

The methodologies employed in this study attempt to capture the phenomenon of the UHI and of intra-urban temperature differences at both skin (land surface) and screen (air) levels. These levels may differ in terms of the media sensed and the predominant physical processes (Arnfield, 2003), so investigating the UHI from seemingly divergent perspectives may provide additional insights.

2.1 | Study area

Located on the fringes of the Negev Desert, Be'er Sheva (31°15′32″N, 34°47′59″E, 260 m MSL) is the largest city in southern Israel, with a population of approximately 210,000 and covering an area of 54 km^2 (Figure 1). The climate is hot semi-arid/arid (Bsh/Bwh according to the Köppen classification) with an average annual rainfall of 195 mm. The maximum daily average temperature is 16.7°C during winter (January) and 32.7°C summer (July). The minimum daily average temperature ranges from 6.0 to 18.5°C in winter and summer, respectively (Bitan and Rubin, 1994).

2.2 | Mobile traverse

The route of the traverse was designed to go through the major urban land use categories, including a low-rise light industrial zone, the central business district, an urban park and several residential neighbourhoods, as shown in Figure 1. To coincide with the overpass of the Landsat-8 satellite, the traverse took place at 10–10:30 local standard time, on July 28, 2016.

Air temperature was measured with two fine (American Wire Gauge [AWG] 34) thermo-couples (type T). Accuracy after calibration in the laboratory was better than ±0.1°C. The thermocouples were placed in a mechanically aspirated shield, constructed from a 10 cm plastic tube wrapped with aluminium foil to protect the thermocouples from direct radiation. The shield was mounted approximately 30 cm above the rooftop of a car (Figure 2). A CR23X Campbell Scientific data logger was used to collect the data at 1 s intervals from which 5-s averages were calculated. The location of each measurement was recorded and time-stamped by Global Positioning System (GPS).

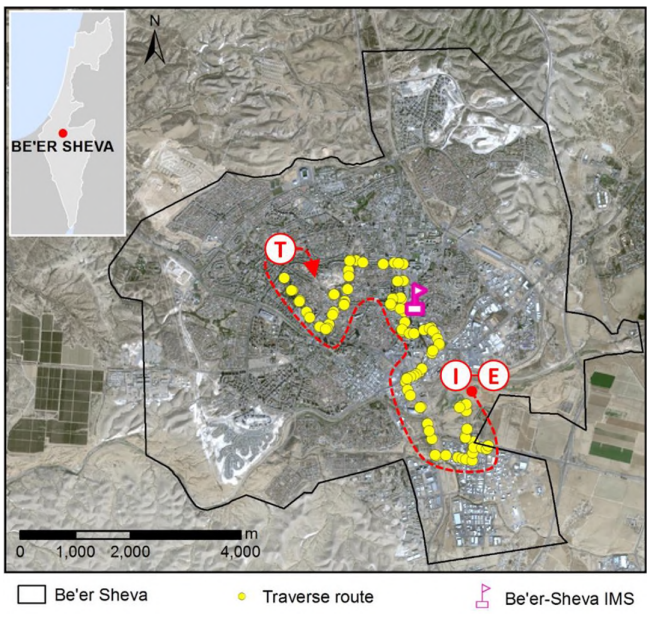

FIGURE 1 Location of Be'er Sheva in Israel (inset), the weather station of the Israeli Meteorological Service (IMS) within Be'er Sheva, and the mobile traverse route on July 28, 2016, with initial (I), turning (T), and end (E) points marked

Although an attempt was made to maintain a constant driving speed, we could not avoid fluctuations caused by traffic, stoplights, etc., which were later shown to result in an increase in temperature due to air stagnation and heat from cars nearby. To estimate the magnitude of air temperature variations data were compared to co-temporal data from the Be'er Sheva Israel Meteorological Service (IMS) station.

2.3 | CAT simulation

An updated version of the Canyon Air Temperature (CAT) model (Erell and Williamson, 2006) incorporating effects of soil moisture on the surface energy balance (SEB) (Leaf and Erell, 2017) was used to generate urbanized descriptors of meteorological conditions, primarily air temperature, in Be'er Sheva. The model, which is described at the scale of street canyons, uses urban canyon 3D geometry (height and width), land cover (fractions of vegetation and water within a 1 km source area), and data from a reference station under similar meso-scale weather to calculate a representative meso-scale base temperature, which is used in turn to calculate the evolution of air temperature at the urban street canyon taking into account the site-specific energy balance. The CAT inputs describing an urban site, and the methods used to estimate them are summarized in Table S1 in the Supplementary Information.

The CAT model was forced using data from the IMS weather station in Nevatim, about 13 km southwest of the city. Data for direct and diffuse radiation, which are not measured at the IMS station, were taken from a weather station at Ben-Gurion University.

To support model application to a city scale, a method was required to automate data acquisition for multiple locations, each representing one cell in a grid. The method, integrating geographical information system (GIS) data sets and remote sensing images, was demonstrated by Kaplan *et al.* (2016), and is extended and improved in the present implementation.

2.3.1 | Urban geometric variables

The CAT simulation requires a description of the geometry of urban street canyon, that is, building height, street

FIGURE 2 Two type T thermo-couples mounted on the rooftop of a car at about 2 m height (a) and the thermo-couples shielded in a mechanically aspirated 10 cm plastic tube (b)

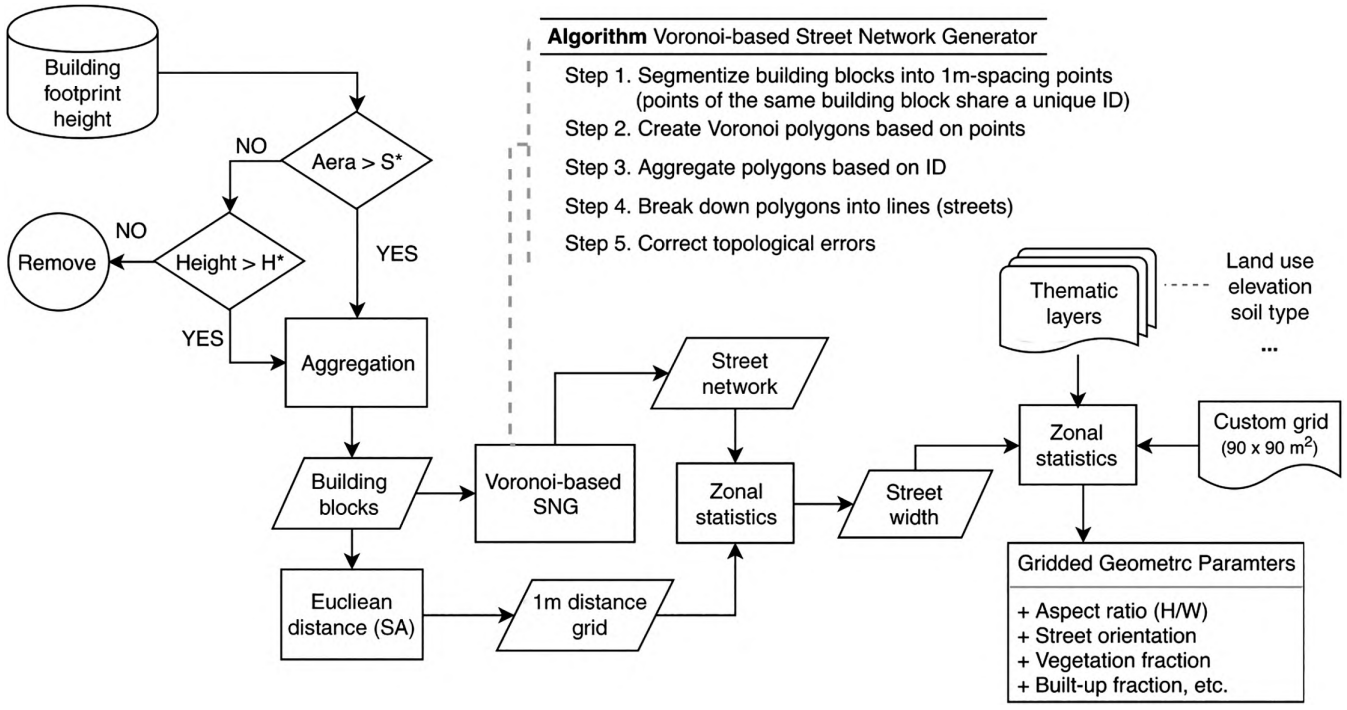

FIGURE 3 Schematic diagram of generating street network based on a geo-database of building footprint/height and the procedure to derive urban geometric parameters required as input in the CAT

width, and orientation. We estimated those variables based on a database of building footprints, using the R software (R Core Team, 2014), and ArcGIS 10.6 (Esri, 2018).

Street width

Street width is defined by the space between building facades on opposite sides of the street, and can be estimated using GIS-based methodology (Kaplan *et al*., 2016). However, as road pavements are not bound to lie in the centre of urban street canyons, the method applied in Kaplan *et al*. (2016), which relies on street centrelines is prone to underestimate the street width. Given that an urban street canyon (defined for the purpose of microclimatic analysis) can be formed even if there are no discernible pavements between

adjacent building blocks, we refined the method to identify street canyons relying only on detailed inputs of building footprints (see Figure 3).

Small low-rise buildings such as kiosks (the criteria being footprint area < 50 m^2 and H < 10 m) that do not contribute to the definition of urban street canyons were filtered out. The remaining buildings within a 15 m radius to each other are iteratively aggregated into continuous building blocks that we regard as the basic elements of an urban street canyon.

Using the building blocks layer as input, the Euclidean Distance Tool in ArcGIS 10.6 (Esri, 2018) was implemented to generate a 1 × 1 m^2 resolution grid, which gives the distance from each raster cell to the closest building block. The distance raster reaches its local maxima along the centreline between any two adjacent building blocks. The set of local maxima constitutes the de facto urban streets.

To identify these local maxima, we proposed a Voronoi-diagram based street network generator which is realized using the *R sf* package (Pebesma, 2018). The algorithm partitions the entire area of interest (Be'er Sheva) into collectively exhaustive and mutually exclusive regions centred at each building block (Okabe *et al.*, 2000). Each region is a collection of points closest to the centred building block, whereas adjacent regions overlap only on their boundaries, forming a tessellation. In our case, the boundaries coincide with the local maxima and thus represent the street network. The resulting street network is subsequently superimposed with the distance grid generated beforehand to compute the street width (see Figure 4).

As the distance from the centreline represents only half of the street, the real street width is double the local maxima. Taking into account site-specific street characteristics, we introduced a minimum threshold of 10 m, that is, only linear spaces wider than 10 m are regarded as streets in Be'er Sheva. If a grid cell has more than one street, CAT uses a street width equal to the average of all streets within it. A street canyon is thus defined as an "edge" consisting of a straight segment of the network of linear urban spaces between two adjacent nodes.

Street orientation

The street orientation (azimuth) is determined based on the de facto urban streets delineated above. Each segment connecting two adjacent junctions is projected onto the cardinal directions, with the north having a value of 0° (see Figure 5a,b). Due to the symmetry of the street orientation, we restricted the orientation angle to 0–180°. The street orientation of a grid cell is determined by the vector mean of street vectors within it (see Figure 5c).

Building height

The database of building footprints provides the height of each building as well. For each grid cell, the mean building height is calculated by averaging heights of buildings,

FIGURE 4 Satellite image from Esri. WorldImagery (Esri, 2019) for a selected urban quarter in Be'er Sheva (a) and the OpenStreetMap layer (OpenStreetMap contributors, 2017) presenting various geographic entities for the same region (b). (c) Building blocks consisting of buildings standing close (<15 m) to each other and the generated Voronoi tessellation representing the street network. (d) The street network superimposed on the 1 × 1 m^2 distance grid to derive street width

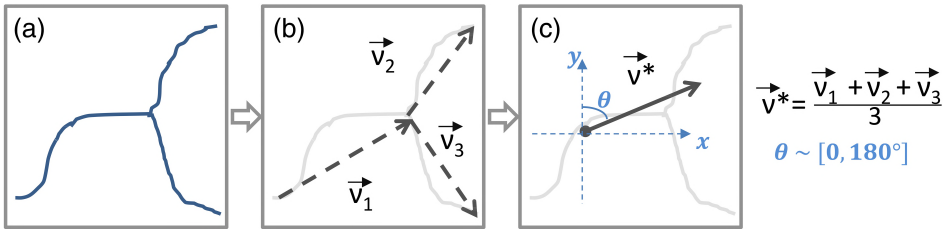

FIGURE 5 Illustration of the derivation of street orientation within a grid cell. (a) and (b) Segments of streets are projected onto the cardinal directions, with the north having a value of 0°. (c) The street orientation of a grid cell is determined by the vector mean of street vectors within it

weighted by their façade wall areas (building footprint circumference × height). For grid cells free of buildings, that is, open space, we set the building height to a minimum value of 3 m and the street width to a maximum of 150 m, which corresponds to a sky view factor of 0.99.

2.3.2 | Anthropogenic heat

The urban SEB includes anthropogenic heat, primarily heat emitted from buildings and from vehicle traffic. In early versions of CAT, this component of the SEB was derived from estimates obtained in other cities by a variety of methods, either top-down or bottom-up. Values used were monthly city-wide averages, included in the CAT input files, which were then processed to generate a typical diurnal profile at hourly time steps. This method was satisfactory for simulations in one urban site, provided an appropriate estimate of the urban average anthropogenic heat was available. The method is not capable, however, of describing intra-urban variations of heat emissions.

Here we propose a methodology to account for differences in emissions among neighbourhoods of different density, at hourly time steps. It uses building height to estimate heat losses by conduction through facades, employing typical thermal properties of walls and windows. To simplify the calculation procedure, conduction at each time step is assumed to be proportional to the difference in air temperature between the building interior (25°C in summer [June–September], 18°C in winter [December–February], and 22°C in transitional seasons [March–April, October–November]) and exterior. Heat transfer by convection is estimated assuming a fixed number of air changes per hour between the interior and the exterior, again based on the difference between internal and external air temperature. The building volume is estimated from its height and assuming a fixed depth (measured from the street façade) of 10 m. The number of air changes per hour is fixed at 1.5, an estimate that is based on the construction quality and airtightness of fenestration in Israel. In summer, heat ejected by air conditioners is assumed to be proportional to the difference in air temperature between the interior and exterior.

Heat emitted by automobiles is estimated as the product of the heat emitted by an average car—3,795 J/m (Sailor and Lu, 2004)—and the number of vehicles travelling down the street. As the latter number is very difficult to obtain, we simply assigned automobile traffic to the street in a given location based on street width (broad streets have higher traffic) and time of day. The diurnal hourly profile accounts for a minimum load at night, maximum load during the morning and afternoon peak hours, and intermediate loads at other times.

For more details on the estimate of the total anthropogenic heat, we refer to Section S2 (Tables S1–S2, Equations S1–S4) in the Supplementary Information. Specifically, Figures S1 and S2 illustrate the diurnal profile of the traffic-related ant the total anthropogenic heat, respectively. Figure S3 shows the gridded total anthropogenic heat for Be'er Sheva in summer and winter.

2.3.3 | Land use and land cover fraction

The CAT model requires a spatially explicit description of vegetation and water fractions in each grid cell and its vicinity. These fractions account for the advection of moisture from source areas that are defined by wind direction and stability (Erell *et al.*, 2009, 2010). The vegetation fraction was estimated from Sentinel-2 images at 20 m resolution using an unsupervised maximum likelihood classifier. Initialized with 50 land use/land cover classes, the identified classes are later collapsed into four types: pavement, buildings, desert (exposed soil), and vegetation. The city of Be'er Sheva has no significant water bodies. The classification achieves an overall accuracy of 0.916 and a coefficient of agreement (Kappa) of 0.839 (for more details see Table S4 in the Supplementary Information).

Following the methodology described in Erell *et al.* (2009) and Kaplan *et al.* (2016), the vegetated fraction of each wedge is calculated based on the gridded land

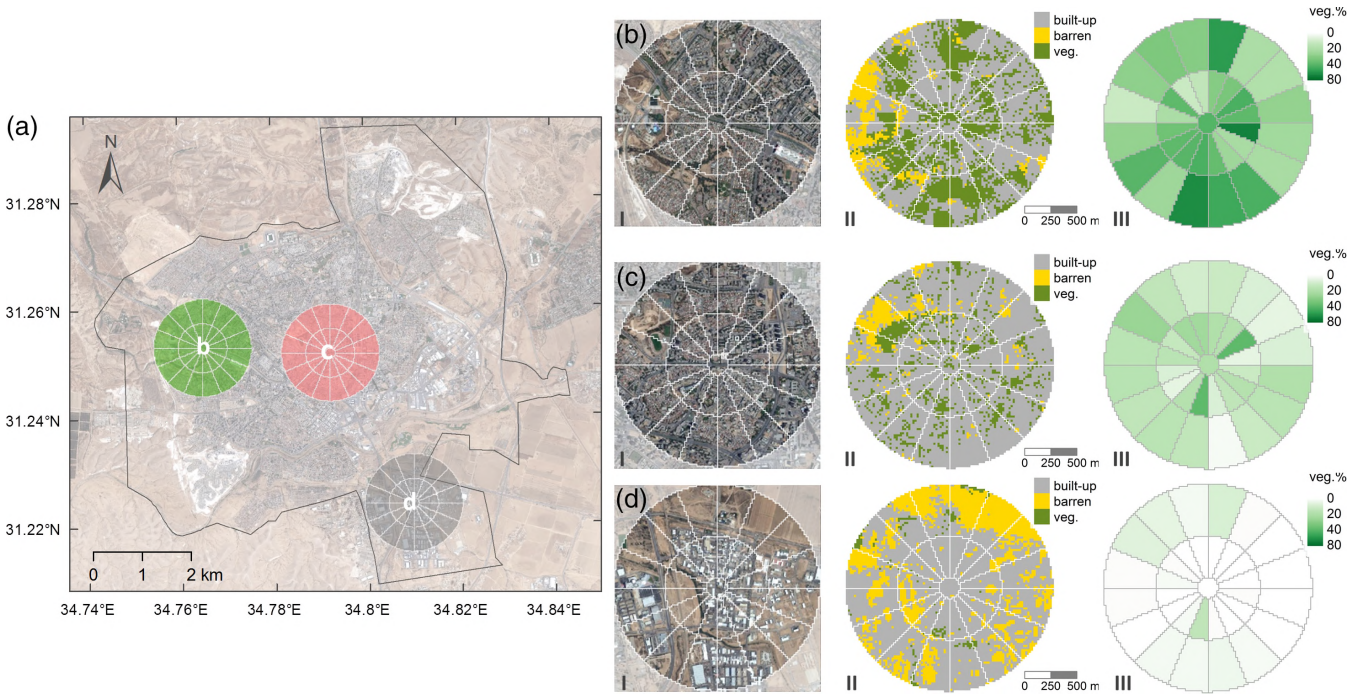

FIGURE 6 Configuration of wedges (a) and satellite images from Google Earth (I-th panel of b–d) for selected grid cells in Be'er Sheva: (b) a residential area with a relatively high fraction of vegetation, (c) the densely built old city quarter, and (d) the sparsely vegetated light industry zone. As Be'er Sheva has scarcely any surface water, the availability of moisture for the centred cell is mostly restricted by the vegetation fraction of the wedges windward, and their values (III-th panel of b–d) are derived from the land cover map (II-th panel of b–d)

use/land cover map generated above. Figure 6 illustrates the configuration of wedges for selected zones in Be'er Sheva which are distinguished from each other in terms of land use, built-up density, and vegetation fraction.

2.3.4 | Surface albedo

A Landsat 8 image on July 28, 2016 was used to estimate albedo with an empirical formula previously developed for the Landsat Thematic Mapper/Enhanced Thematic Mapper Plus (TM/ETM+) sensor (Liang, 2001):

$$\alpha = 0.356*b2 + 0.13*b4 + 0.373*b5 + 0.085*b6 + 0.072*b7 - 0.0018,$$

where b2, b3, b4, b5, b6, and b7 correspond to the reflectance in Landsat-8 spectral bands 2 (0.45–0.515 μm), 3 (0.525–0. 60 μm), 4 (0.63–0.68 μm), 5 (0.845–0.885 μm), 6 (1.560–1.660 μm), and 7 (2.1–2.3 μm), respectively. The building footprints are then masked, and the mean ground surface albedo for each grid cell is calculated and incorporated into the CAT model. The average albedo values of each 90 m grid cell were found to range from 0.11 to 0.53.

2.4 | Thermal remote sensing

Contiguous LST data can be derived from remotely sensed thermal infrared satellite images. In order to compare and contrast the mobile traverse measurements, we used a Landsat-8 scene acquired at 08:11 UTC (about 10:11 local standard time) on July 28, 2016. Landsat 8 thermal band 10 (10.6–11.2 μm), which is registered and resampled to 30 m resolution using a cubic convolution from the original 100 m collection, was used to estimate LST following USGS (2016):

$$T_B = \frac{K2}{\ln\left(\frac{K1}{L_\lambda + 1}\right)},$$

where T_B is the Top of Atmosphere (TOA) Brightness Temperature in Kelvin; K1 and K2 are band-specific thermal conversion constants from the metadata. For Landsat-8 band 10, K1 and K2 are 774.8853 and 1,321.0789, respectively. L_λ denoting the TOA spectral radiance in $W \cdot m^{-2} \cdot sr^{-1} \cdot \mu m^{-1}$, is converted from pixel digital numbers from band 10 using $L_\lambda = M_L DN + A_L$, where M_L and A_L represent the band-specific multiplicative and additive rescaling factors from the metadata (for Landsat-8 band 10, M_L and A_L are 3.3420E-04 and 0.1, respectively).

TABLE 2 Land surface emissivity estimated empirically for each land cover class

	Roads	Built-up	Desert (sand)	Vegetation (grass)
Emissivity (ε)	0.94	0.94	0.95	0.98

To account for emissivity (ε) of different land covers, we corrected the brightness temperature to obtain LST following Weng *et al.* (2004):

$$LST = \frac{T_B}{1+\lambda\frac{T}{\rho}\ln\varepsilon},$$

where λ is the wavelength of emitted radiance (10.9 μm for band 10), $\rho = h\sigma/s$ (1.4388E−02 m·K), σ = Boltzmann constant (1.38E−23 J·K^{-1}), h = Planck's constant (6.626E−34 J·s), and c = velocity of light (2.998E−08 m·s^{-1}). The values of surface emissivity (Table 2) are empirically estimated based on the land use and land cover classification generated previously (Qin *et al.*, 2005; Yu *et al.*, 2014).

As the UHI is found to be more pronounced at night (Oke, 1987; Runnalls and Oke, 2000) and the Landsat-8 does not provide night-time images, we also used images from the Advanced Spaceborne Thermal Emission and Reflection Radiometer (ASTER) satellite sensor. With a 90 m resolution, the ASTER surface kinetic temperature (AST_08) product (NASA LP DAAC 2001) provides high resolution images for LST night-time analysis. Given image availability, quality, and cloud coverage, we used an image acquired on July 30, 2012 for analysis. For both day- and night-time images, pixel values were converted from kinetic temperature in Kelvin to degrees Celsius. All data were downloaded from the United States Geological Survey (USGS) website at https://espa.cr.usgs.gov/ordering/new/.

The surface UHI (SUHI) is referred to as the difference of LST between the urban area and its surrounding natural environment. The SUHI was calculated by subtracting the average LST of all desert pixels outside the city border within a region of interest which matches approximately the extent of Figure 1. Mean desert LST when the satellite was overhead (at 10:00 local time on July 28, 2016, the date of the traverse) was estimated at 41.1°C.

3 | RESULTS

3.1 | Land use classification

The city of Be'er Sheva and its vicinity were divided into a total of 10,400 (100 × 104) grid cells of 90 × 90 m^2. The land use and land cover in Be'er Sheva is characterized as bare, sparsely vegetated open space, which constitutes 39% of the urban administrative area (Figure 7). The shares of buildings, paved roads, and vegetation are 37, 11, and 13%, respectively. The scattered fragments of vegetation within the city and the larger green patches at the city's western periphery are drip-irrigated urban greening and jojoba fields at Kibbutz Hazerim, respectively.

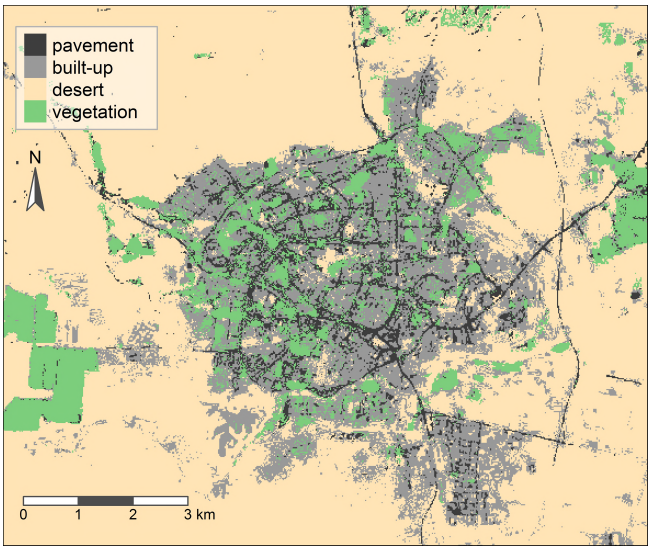

FIGURE 7 Land use and land cover map for Be'er Sheva using an unsupervised maximum likelihood classifier

3.2 | Urban geometric parameters

The linear spaces ("streets") identified using the methodology described above are aggregated at the grid cell level to derive the average street width and orientation, which are shown in Figure 8b,c. As shown in Figure 8a, Be'er Sheva is dominated by low-rise to mid-rise buildings with a height of less than 30 m. Some medium- to high-rise residential buildings are found in the south-western part of the city. Except in the old city and several old urban quarters, streets are often wide (median of 42 m, irrespective of open spaces).

The relatively low building height alongside the large street width results in a generally low aspect ratio (H/W) of urban street canyons. Of 3,325 urban cells, 78.6% have an aspect ratio smaller than 0.5 (avenue canyon), while only 13 cells have a value larger than 2 (deep canyon). Be'er Sheva has an irregular grid of streets with a predominance of east-oriented streets at the grid cell level.

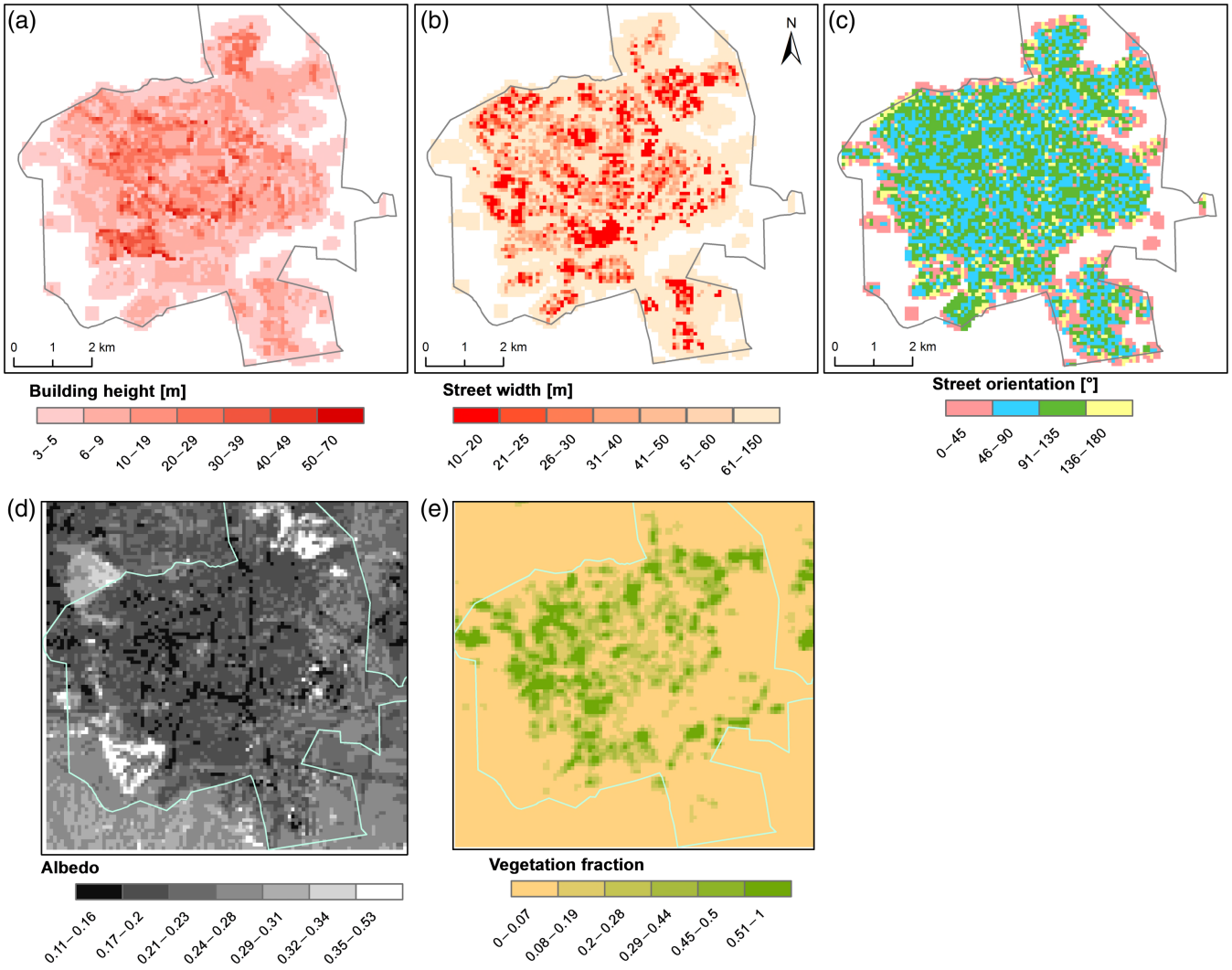

FIGURE 8 Spatial distributions of selected CAT-parameters in 90 × 90 m^2 grids: (a) building height, (b) street width, (c) street orientation, (d) albedo, and (e) vegetation fraction. The parameters in the upper panels (a)–(c) are derived from a building footprint geodatabase. Therefore, values are only calculated for grid cells containing buildings

3.3 | Evaluation of CAT simulation

Model performance was assessed by comparing the predicted and observed values of an Israel Meteorological Service weather station located inside the urban area (31.251433 N, 34.799420 E, 280 m mean sea level [MSL]). As shown in Figure 9, the land cover within the station is bare soil, and it is surrounded by vegetation and small low-rise buildings.

Since CAT performs a modification of the regional air temperature to estimate a local value, the temperature from the reference station may itself be a fairly good approximation of the object of the simulation (Figure 10). The model may thus only be considered useful if the simulation output is closer to the observed value than this input. Model performance was estimated using the Williamson Degree of Confirmation—DoC (Williamson, 1995). In addition, standard measures such as the root mean square error (RMSE) as well as more sophisticated ones recommended by Moriasi *et al.* (2007), Willmott (1981, 1982) and Willmott *et al.* (1985) were used for model evaluation.

Statistical measures of model performance are shown in Table 3. The model has a root mean square error of 0.89°C and a DoC of 0.232, indicating that the CAT model has an overall good performance and is able to estimate urbanized air temperature better than simply using temperature measurement from a rural reference under similar meso-scale weather conditions.

Moriasi *et al.* (2007) also suggest that *"In general, model simulation can be judged as satisfactory if Nash–Sutcliffe efficiency index (NSE) >0.50 and RMSE-observed standard deviation ratio (RSR) <0.70..."* and in addition that model bias should be below certain thresholds that are determined based on the uncertainty of the measured

FIGURE 9 The site of the urban weather station (a) with a Stevenson screen (b) in the centre of Be'er Sheva operated by the Israeli Meteorological Service (IMS)

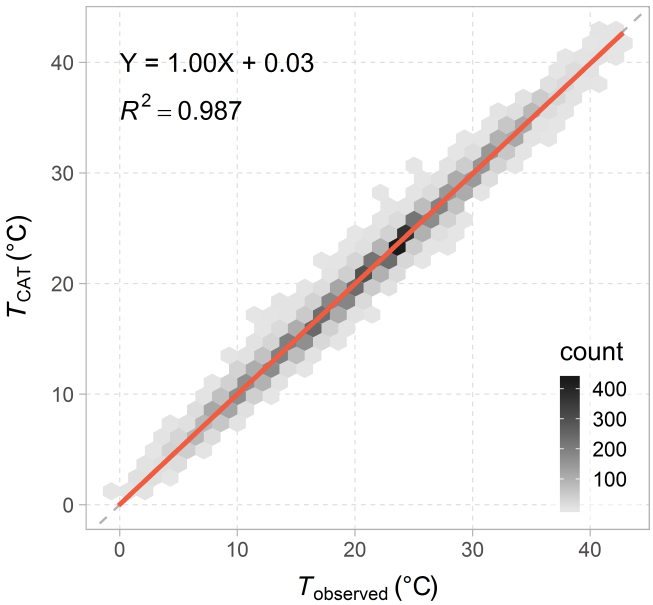

FIGURE 10 Scatterplot showing hourly modelled (TCAT) and observed near-surface air temperature (T observed) for 2016 (8,784 hourly values). There is a good agreement overall with a best-fit regression line having a slope of unity and a negligible offset

TABLE 3 Statistical evaluation of the predicted surface air temperature

Total number of hours	8,784
Mean error	0.04
SD of error	0.89
Maximum error	4.36
Minimum error	−5.89
Root mean square error	0.89
Systematic root mean square error	0.05
Unsystematic root mean square error	0.89
Willmott index of agreement	0.99
Williamson degree of confirmation (DoC)	0.232
Nash–Sutcliffe efficiency index (NSE)	0.987
Percent bias (PBIAS)	0.19
RMSE-observed *SD* ratio (RSR)	0.113

data. The model in this study achieved an NSE of 0.987 and an RSR of 0.113, exceeding the suggested values of a satisfactory model.

Figure 11 illustrates model performance for two periods of several days each in January and July, respectively. The upper panel shows a winter period beginning with overcast weather followed by a rainy day on 25th January and in the mid-morning of 26th January. Changes in soil moisture and the latent flux following the rain are reflected in model output, as the surface temperature over the subsequent days is substantially lower than in the preceding period. However, during strong wind spells (marked with grey dashed rectangle) and in the initial phase of rain events (with blue dashed rectangle), the CAT model is prone to underestimate air temperature for the urban station. We hypothesize that this divergence could be associated with two factors: (a) rain events in the desert are often observed localized over a relatively small region, which may put into question the basic assumption of CAT that similar meso-scale weather exists between urban and rural stations; and (b) the increased roughness of urban built-ups results in reduced wind speed in cities. The CAT model is able to account for the wind effect on air temperature at low wind speeds but becomes less capable during strong wind gust.

3.4 | Spatio-temporal pattern of intra-urban temperature variability

Figure 12 shows the spatio-temporal pattern of modelled UHI in Be'er Sheva at 6 hr intervals on a typical winter day

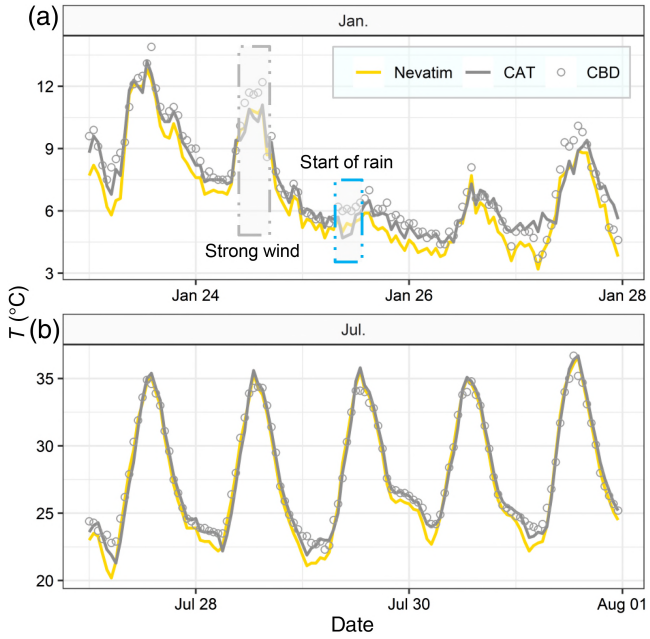

FIGURE 11 Time series of observed (urban station in points and rural reference in Nevatim) and CAT-simulated near-surface air temperature of the urban station for two periods in January (a) and July (b). (a) A strong wind spell and the initial phase of a whole-day rain event, in which CAT underestimated surface air temperature, are marked with dashed rectangles

(January 20, 2016) and a summer day (July 28, 2016). In this study, the UHI intensity is defined as the temperature difference of each urban cell relative to measurement from the rural reference station in Nevatim. For both winter and summer days, Be'er Sheva exhibits a more pronounced UHI during night-time than daytime. The maximum nocturnal UHI reached about 4°C in the winter and diminished to about 2°C in the summer, while the daytime UHI was usually less than 1°C. However, a weak cool island, that is, urban cells are cooler than the rural reference, could appear in the mid-morning shortly after the sunrise, as exposed desert surfaces heat more rapidly than urban surfaces of higher thermal mass.

To check whether the cool island is also present in other periods of the year, we calculated hourly mean UHI by averaging the UHI of all urban cells at each hour. As shown in Figure 13, the urban cool island was also widely present based on the modelled surface air temperature throughout the year, predominantly in the period between sunrise and noon.

3.5 | Comparison between traverse measurement and CAT simulation

Figure 14 compares surface air temperature modelled by CAT and measurements recorded by the vehicular

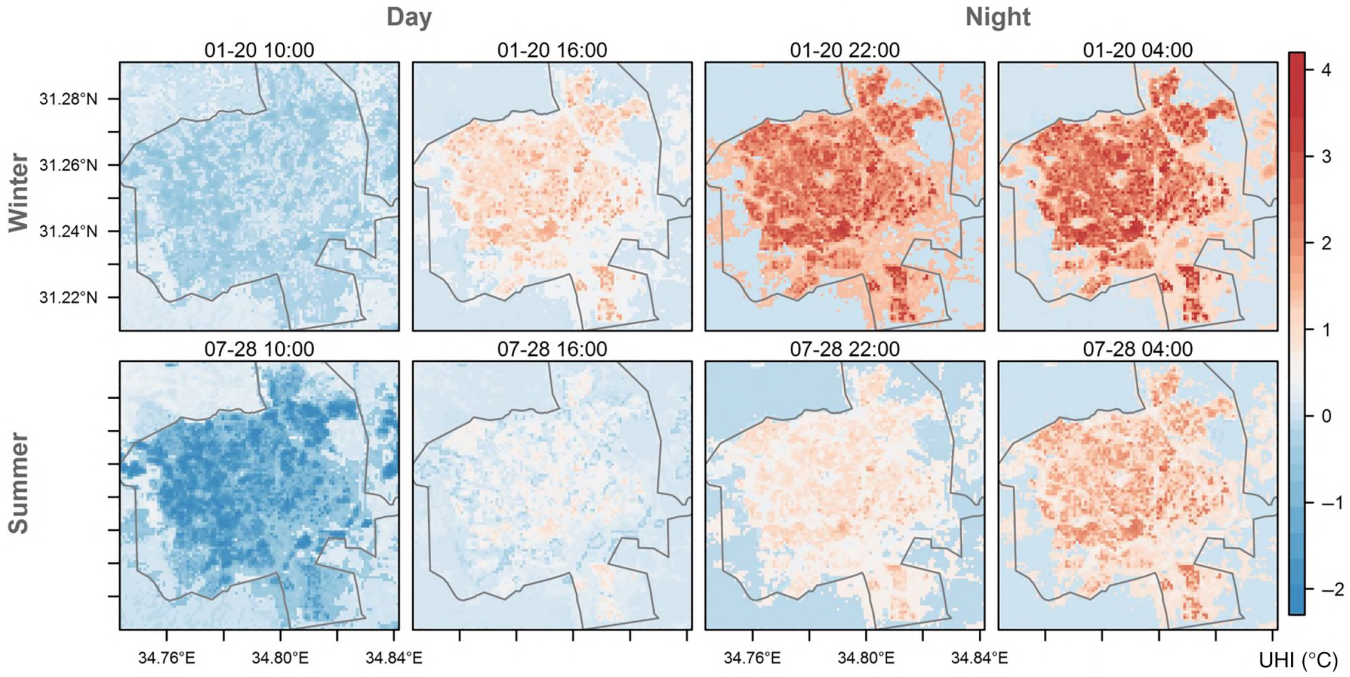

FIGURE 12 Spatio-temporal pattern of modelled surface air temperature at 6 hr intervals on a typical winter day (January 20, 2016) and summer day (July 28, 2016), grouped in daytime (LT1000 and 1,600) and night-time (LT2200 and 0400). The UHI intensity is defined as the temperature difference relative to the rural reference measurement

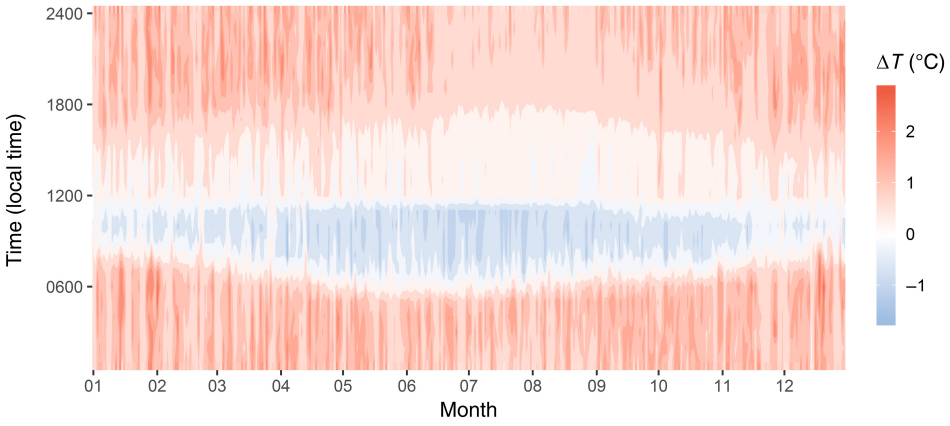

FIGURE 13 Temporal pattern of the mean UHI in Be'er Sheva, modelled at hourly time steps. A weak cool island may be observed in Be'er Sheva from sunrise till noon

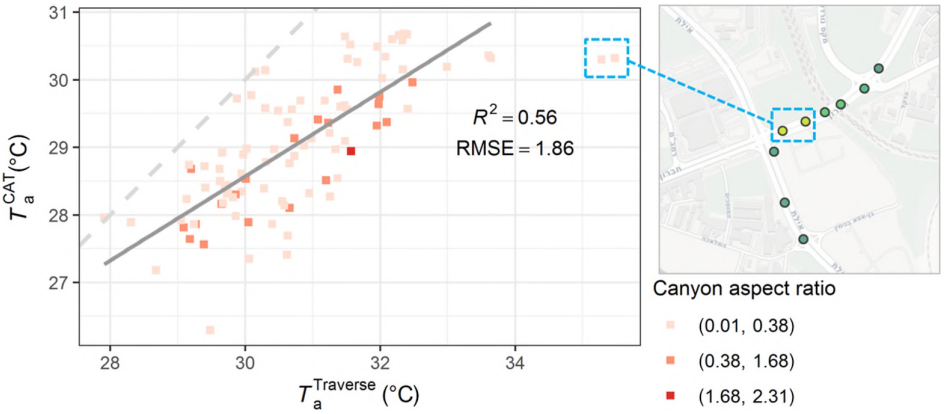

FIGURE 14 T_a simulated by CAT versus the traverse vehicular measurement in the mid-morning (about 10:00 local time) on July 28, 2016. The 2 points with abnormally high T_a were measured during stops at red lights at the road junction

traverse in the mid-morning of July 28, 2016. At first glance, the CAT model seems to underestimate surface air temperature in urban street canyons. However, we have to highlight several sources of model error which may account for the discrepancy. Firstly, the attempt to maintain a constant driving speed during traverse measurement often fails in urban settings due to complex traffic conditions, for example, stops at traffic lights, traffic jams. As a consequence, heat may accumulate during stops at junctions, resulting in abnormally high temperature measurement. This could explain the two outlier measurements in Figure 14.

Secondly, the CAT model incorporates an incomplete description of processes happening simultaneously in cities. As described in Section 2.3.2, traffic-related heat is estimated using a simplified approach rather than taking into account real-time traffic counts. Thirdly, systematic errors resulting from measuring instruments (e.g., sensors, installation of shields) could also introduce bias to the measurement.

Lastly, the CAT model outputs hourly mean surface air temperature of a grid cell (in this study 90×90 m^2) represented as a street canyon, thus takes only limited account of the heterogeneity inside the cell. In comparison, the mobile traverse measures real-time temperature signals at a certain place and a certain time. As the sky view factor is relatively high in urban street canyons in Be'er Sheva, streets are scarcely shaded and directly exposed to the sun most of the time during the day. This makes streets often hotspots within a cell during daytime, exhibiting a higher temperature than the mean of the cell where they are located.

3.6 | Surface UHI

Figure 15 demonstrates the variability of surface skin temperature (T_s) in the city and its vicinity by means of night-time ASTER (a) and daytime Landsat-8 (b) images, respectively. Night-time surface skin temperature shows a SUHI (definition see Section 2.4) of 4–5°C, in contrast to a cool island of similar magnitude in mid-morning (approximately 10:00). The bare desert soil (loess) in the suburbs and urban periphery has a low thermal capacity and consequently exhibits large changes in temperature—cooling down rapidly after sunset but also heating up very rapidly after sunrise. This explains the anomalous dirunal pattern of a paved road junction (black dashed circle) in the urban

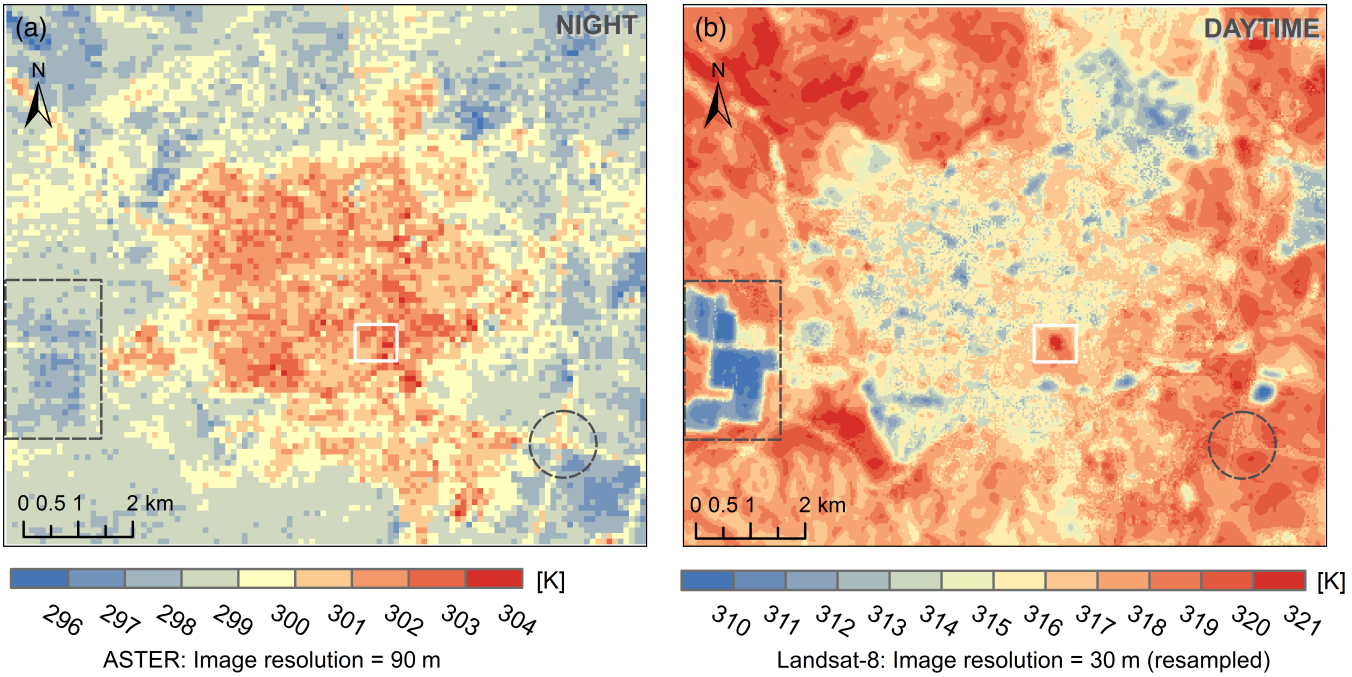

FIGURE 15 Surface kinetic temperature captured by (a) the ASTER sensor at 90 m resolution for night-time at about 22:00 local time July 30, 2012 and (b) the Landsat-8 satellite at 30 m resolution (resampled) for daytime at about 10:00 local standard time July 28, 2016. Night-time surface skin temperature data show a SUHI of 4–5°C, in contrast to a cool island of similar magnitude in mid-morning (approximately 10:00). The dashed rectangle, solid rectangle, and dashed circle mark an irrigated jojoba farm, a cemetery and a road junction, respectively, which exhibit abnormal temperature pattern in contrast to their surroundings

periphery in contrast to the desert surrounded. The hotspot near the centre of the daytime image (white rectangle) is a bare soil Moslem cemetery, and thus behaves rather like open desert. As a comparison, an agricultural field on the western urban fringe (grey dashed rectangle) presents a constant cold spot at both day- and night-time, which highlights the cooling effect of irrigated vegetation in semi-arid/arid regions.

Figure 16 compares the distribution of the modelled air temperature at 10:00 local standard time July 28, 2016 and the Landsat-8 T_s obtained at the same time for the same area. The two temperatures differ remarkably from each other in terms of conventional descriptive statistics (e.g., value range, mean), posing a great challenge to estimate (usually) air temperature from surface skin temperature.

Constrained by data availability, we applied the Temperature-Vegetation Index (TVX) approach using the daytime Landsat-8 T_s data, to derive the corresponding T_a. The TVX approach assumes a negative correlation between T_s and vegetation indices such as normalized difference vegetation index (NDVI), and that T_a is in equilibrium with T_s of infinitely thick vegetation canopy, that is, at a very high NDVI value (Prihodko and Goward, 1997). We applied a moving window of different size and different maximum NDVI as summarized in Zhu *et al*. (2013).

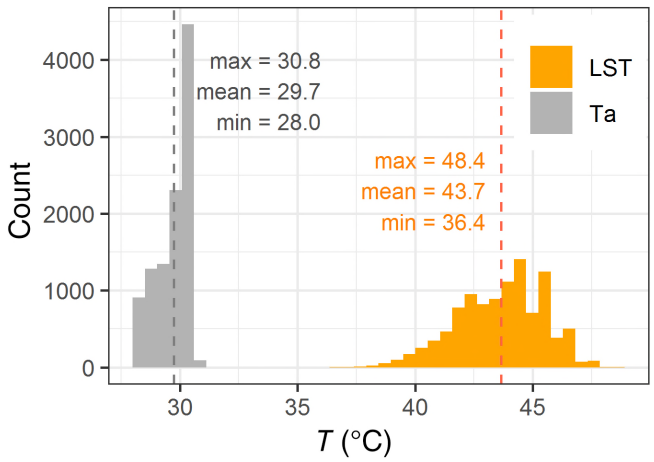

FIGURE 16 Histogram of T_a modelled by CAT at 10:00 local standard time July 28, 2016 and the corresponding daytime LST for the same area. The latter is aggregated to 90 m resolution and consistent with the former

However, the method seems not to work properly in desert conditions, as a negative correlation between T_s and NDVI does not always hold in the morning. In bare unvegetated areas outside the city, the correlation is mostly positive. The regression in the TVX might

generally fail for desert regions where NDVI is small in both value (with a mean of 0.11) and range (with a *SD* of 0.03).

Moreover, factors like albedo are also observed to have an impact on the variability of T_a. Limestone bedrocks common in the Negev desert normally exhibit a lower temperature than the surrounding bare soil, which is ascribed to a higher albedo associated with the light colour of the former.

4 | DISCUSSION

The following section first describes the limitations of each of the three methods employed, as experienced in this study. The implications of these limitations are then illustrated in the context of the particular characteristics of a desert city.

The *traverse* was performed by automobile and was limited to paved roads. Thus, passing at a street adjacent to a small urban park was not reflected in the temperature measurements, because the (assumed) cooling effect of the park did not extend to the road. As the response time of the thermocouples was rapid, the temperature record captures transient turbulence manifested in temperature fluctuations of as much as 1°C or more. Averaging the readings over 5 s may not smooth out such temperature fluctuation. A longer averaging period, sufficient to reduce the effect of such micro-scale turbulence, would have resulted in the loss of spatial detail: a vehicle travelling at 50 $km \cdot hr^{-1}$ will traverse a 100 m wide park in less than 8 s. In contrast, stopping at traffic lights for 1–2 min exposed the vehicle to exhaust fumes of adjacent automobiles, resulting in elevated temperature readings that were most likely very localized (they were not apparent in data points recorded before the intersection or after it) and possibly transient. The temperature data recorded during the traverse are therefore "accurate" in a narrow technical sense—but are they necessarily representative of a larger spatial extent or a longer time?

At the other spatial extreme, *remote sensing* can quantify the magnitude and spatial extent of UHI and enable comparison of UHIs among different cities at continental scales (Imhoff *et al*., 2010; Zhou *et al*., 2013). However, it is still incapable of resolving micro-scale features of the urban landscape. It is also limited to clear sky conditions. If the objective of a study is to inform localized decision making, the spatial averaging displayed in images derived from the satellite infrared sensing limits their utility.

Finally, despite an overall acceptable performance of the CAT *model*, we should acknowledge a limitation of CAT, namely that the model may be applied only where the city and the rural reference station are exposed to similar meso-scale weather conditions. If this condition is not satisfied, due to weather events that have significant dynamics but very localized impacts (e.g., wind gusts or torrential local rainfall), the model will generate biased urbanized air temperature proximate to the rural reference (as shown in Figure 11a). The pros and cons of the grid based approach used in this study have been discussed in detail previously in Kaplan *et al*. (2016): In short, the gridded version of CAT model achieves a computational efficiency in simulating the intra-urban variation of microclimate at the cost of an incomplete description of the heterogeneity of 3D characteristics within each urban cell. Setting a large grid cell size could lead to an over-homogenization that fails to capture the spatial variation of urban microclimate. Therefore, small cell size is preferred. Meanwhile, each grid cell is conceived as a unique urban street canyon that should encompass at least a street of sufficient length. These competing requirements demand a high level of sophistication on the configuration of a grid of appropriate cell size—the cell should be set as small as possible, but not smaller.

The application of the three methodologies in the study of Be'er Sheva yielded insights which would not have been observed individually. The existence of a modest daytime cool island in dry cities has been noted in the past through localized ground observations of air temperature (Erell and Williamson, 2007) and remote sensing of LST (Peng *et al*., 2012; Lazzarini *et al*., 2015; Shastri *et al*., 2017). However, the temporal persistence and spatial extent of the air temperature cool island modelled by CAT (Figures 12 and 13), though not unexpected, have not been reported in studies of the urban climate. Similarly, although anthropogenic heating due to air conditioning has been modelled at an urban scale using WRF (Salamanca *et al*., 2014), the present study introduces a framework to resolve anthropogenic sources at a higher spatial resolution (see Supplementary Information for details). Although we do not have flux measurements to validate the predicted values, it is encouraging to see the correlation between known "hotspots," such as closely built high-rise buildings, and hotspots illustrated by the simulation. The mean annual value for the urban area obtained by this method is approximately 22 $W \cdot m^{-2}$, similar to values obtained by Sailor *et al*. (2015) for Rome, Italy, which has similar heating and cooling requirements and a similar population density.

Comparison of the findings from the present study with previous research illustrates the effect of methodology on the findings. Time series analysis of urban air temperature in comparison with a rural location west of Be'er Sheva by Saaroni and Ziv, 2010 reported a persistent UHI of 3.0 to 0.8°C in summer (daily minima and

maxima, respectively), and 2.0 to 1.5°C in winter. Mandelmilch *et al.* (2019), in contrast, who investigated the characteristics of LCZs in Be'er Sheva using short term measurements, reported that the UHI is more significant in winter than in summer, and that the summer UHI is larger during daytime than at night. Unlike some computational studies of desert cities (e.g., Zhao *et al.*, 2014), neither paper reported a daytime near surface cool island. This may be due to the location of the measurement sites (Saaroni and Ziv (2010) selected a reference station that is west of Be'er Sheva and closer to the moderating influence of the Mediterranean Sea), or to the use of minimum and maximum temperatures for comparison, rather than hourly values throughout the day.

5 | CONCLUSIONS

Three different methods were applied to investigate the intra-urban microclimate variability of a desert city at both screen (air temperature) and skin (surface skin temperature) levels, namely in-situ measurement from fixed weather stations and vehicular traverse, computer simulation, and satellite-borne remote sensing. We find that the results obtained by different methods used for evaluating the urban climate might not be consistent with each other. Consequently, while we do not necessarily rule out conclusions and suggestions drawn from studies based exclusively on a single method, we suggest that such studies should be interpreted much more carefully. As our study has demonstrated, urban–rural differences in LST obtained by remote sensing may be substantially larger than concurrent differences in canopy layer air temperature, at night as well as in daytime. Similarly, differences in vegetation cover among urban neighbourhoods are clearly visible in images of LST but may generate only moderate differences in air temperature. Policy recommendations based on the impact of vegetation on air temperature alone may in this case underestimate the benefits of green infrastructure, because air temperature is only one of the factors that affect pedestrian thermal comfort and building energy demand.

Computer simulation at appropriate scale may be able to bridge the spatial gap between surface based in-situ measurements, that are inherently local, and remote sensing data, which cannot resolve all thermal fluxes, despite great improvement in resolution and accuracy. This study demonstrates an innovative GIS-based, bottom-up approach to generating the required inputs. The method to derive urban geometric parameters relies on several input layers of moderate resolution, such as land cover, albedo, and building footprints. These data are either publicly accessible, for example, from the Landsat or Sentinel missions, or there are open access alternatives, for example, the Microsoft building footprints data for the United States (Bing maps team, 2018). In combination, they make the method easily applicable in any model requiring a detailed description of urban geometry.

Our findings contribute to the limited sample of existing studies on the temperature dynamics of cities located in semi-arid/arid climate zones. It confirms discrepancies reported in some other desert cities between the surface UHI (LST) observed by remote thermal imaging and ground-based air temperature measurements in the canopy layer. Thus, Be'er Sheva exhibits a daytime surface cool island and a weak but persistent daytime cool island at screen level, as well as the customary nocturnal heat island.

Though different methods may sometimes result in seemingly contrasting outcomes, they serve to complement each other, and should be used in combination to obtain an unbiased description of the spatio-temporal patterns of intra-urban microclimate variability. In contrast to a burgeoning number of studies that rely on remote sensing, the relative paucity of spatially detailed ground-based near-surface air temperature data in cities—highlight the need for more urban microclimate monitoring campaigns. Given the respective advantages and disadvantages inherent in each method, we suggest that a multi-method approach could provide synergistic opportunities to enrich our understanding of the complex land surface-atmosphere interaction.

ACKNOWLEDGEMENTS

This study was funded by the Israel Ministry of Science, Technology and Space, under contract # 63365 and by the Jewish National Fund through the Center for Water Sensitive Cities in Israel. B.Z. was supported by the post-doctoral scholarship of the Kreitman School for Advanced Graduate Studies of the Ben-Gurion University of the Negev and the PBC Fellowship Program for outstanding Chinese and Indian post-doctoral students. S.K. was supported by the Jacob Blaustein Center for Scientific Cooperation.

ORCID

Bin Zhou https://orcid.org/0000-0001-8853-0724

REFERENCES

Arnfield, A.J. (2003) Two decades of urban climate research: a review of turbulence, exchanges of energy and water, and the urban heat island. *International Journal of Climatology*, 23(1), 1–26. https://doi.org/10.1002/joc.859

Baker, L., Brazel, A., Selover, N., Martin, C., McIntyre, N., Steiner, F., Nelson, A. and Musacchio, L. (2002) Urbanization

and warming of Phoenix (Arizona, USA): impacts, feedbacks and mitigation. *Urban Ecosystems*, 6(3), 183–203. https://doi.org/10.1023/A:1026101528700

Bing maps team. (2018) *Microsoft US Building Footprints Data*. Bing maps team.

Bitan, A. and Rubin, S. (1994) *Climatic Atlas of Israel for Physical and Environmental Planning and Design*. Tel Aviv: Ramot Publishing.

Brazel, A.J. and Hedquist, B.C. (2006) Urban, residential, and rural climate comparisons from mobile transects and fixed stations: Phoenix, Arizona. *Journal of the Arizona-Nevada Academy of Science*, 38(2), 77–87. https://doi.org/10.2181/1533-6085(2006)38[77:URARCC]2.0.CO;2

Brazel, A., Selover, N., Vose, R. and Heisler, G. (2000) The tale of two climates—Baltimore and Phoenix urban LTER sites. *Climate Research*, 15, 123–135. https://doi.org/10.3354/cr015123

Bruse, M. and Fleer, H. (1998) Simulating surface-plant-air interactions inside urban environments with a three dimensional numerical model. *Environmental Modelling and Software*, 13(3–4), 373–384. https://doi.org/10.1016/S1364-8152(98)00042-5

Chen, F., Kusaka, H., Bornstein, R., Ching, J., Grimmond, C.S.B., Grossman-Clarke, S., Loridan, T., Manning, K.W., Martilli, A., Miao, S., Sailor, D., Salamanca, F.P., Taha, H., Tewari, M., Wang, X., Wyszogrodzki, A.A. and Zhang, C. (2011) The integrated WRF/urban modelling system: development, evaluation, and applications to urban environmental problems. *International Journal of Climatology*, 31(2), 273–288. https://doi.org/10.1002/joc.2158

Erell, E. and Williamson, T. (2006) Simulating air temperature in an urban street canyon in all weather conditions using measured data at a reference meteorological station. *International Journal of Climatology*, 26(12), 1671–1694. https://doi.org/10.1002/joc.1328

Erell, E. and Williamson, T. (2007) Intra-urban differences in canopy layer air temperature at a mid-latitude city. *International Journal of Climatology*, 27(9), 1243–1255. https://doi.org/10.1002/joc.1469

Erell, E., Eliasson, I., Grimmond, S., Offerle, B., Williamson, T. (2009) Incorporating spatial and temporal variations of advected moisture in the canyon air temperature (Cat) model. In: *The Seventh International Conference on Urban Climate*, (July), pp. 29–32.

Erell, E., Eliasson, I., Grimmond, S., Offerle, B., Williamson, T. (2010) The effect of stability on estimated variations of advcted moisture in the canyon air temperature (CAT) model. In: *The 9th AMS Symposium on the Urban Environment*, (1), pp. 3–8.

Esri. (2018) *ArcGIS Desktop: Release 10.6*. Redlands, CA: Environmental Systems Research Institute.

Esri. (2019) *World Imagery May 15, 2019*.

Georgescu, M., Moustaoui, M., Mahalov, A. and Dudhia, J. (2012) Summer-time climate impacts of projected megapolitan expansion in Arizona. *Nature Climate Change. Nature Publishing Group*, 3(1), 37–41. https://doi.org/10.1038/nclimate1656

Georgescu, M., Chow, W.T.L., Wang, Z.H., Brazel, A., Trapido-Lurie, B., Roth, M. and Benson-Lira, V. (2015) Prioritizing urban sustainability solutions: coordinated approaches must incorporate scale-dependent built environment induced effects. *Environmental Research Letters. IOP Publishing*, 10(6), 61001. https://doi.org/10.1088/1748-9326/10/6/061001

Guhathakurta, S. and Gober, P. (2010) Residential land use, the urban heat island, and water use in phoenix: a path analysis. *Journal of Planning Education and Research*, 30(1), 40–51. https://doi.org/10.1177/0739456X10374187

Hartz, D.A., Prashad, L., Hedquist, B.C., Golden, J. and Brazel, A.J. (2006) Linking satellite images and hand-held infrared thermography to observed neighborhood climate conditions. *Remote Sensing of Environment*, 104(2), 190–200. https://doi.org/10.1016/j.rse.2005.12.019

Imhoff, M.L., Zhang, P., Wolfe, R.E. and Bounoua, L. (2010) Remote sensing of the urban heat island effect across biomes in the continental USA. *Remote Sensing of Environment. Elsevier B.V.*, 114(3), 504–513. https://doi.org/10.1016/j.rse.2009.10.008

Ivajnšič, D., Kaligarič, M. and Žiberna, I. (2014) Geographically weighted regression of the urban heat island of a small city. *Applied Geography*, 53, 341–353. https://doi.org/10.1016/j.apgeog.2014.07.001

Kaplan, S., Peeters, A. and Erell, E. (2016) Predicting air temperature simultaneously for multiple locations in an urban environment: a bottom up approach. *Applied Geography. Elsevier Ltd*, 76, 62–74. https://doi.org/10.1016/j.apgeog.2016.09.015

Kloog, I., Chudnovsky, A., Koutrakis, P. and Schwartz, J. (2012) Temporal and spatial assessments of minimum air temperature using satellite surface temperature measurements in Massachusetts, USA. *Science of the Total Environment. Elsevier B.V.*, 432, 85–92. https://doi.org/10.1016/j.scitotenv.2012.05.095

Kloog, I., Nordio, F., Lepeule, J., Padoan, A., Lee, M., Auffray, A. and Schwartz, J. (2017) Modelling spatio-temporally resolved air temperature across the complex geo-climate area of France using satellite-derived land surface temperature data. *International Journal of Climatology*, 37(1), 296–304. https://doi.org/10.1002/joc.4705

Koohafkan, P. and Stewart, B.A. (2008) *Water and Cereals in Drylands. Water and Cereals in Drylands*. Rome: FAO/Earthscan.

Laaidi, K., Zeghnoun, A., Dousset, B., Bretin, P., Vandentorren, S., Giraudet, E. and Beaudeau, P. (2011) The impact of heat islands on mortality in Paris during the august 2003 heat wave. *Environmental Health Perspectives*, 120(2), 254–259. https://doi.org/10.1289/ehp.1103532

Lazzarini, M., Molini, A., Marpu, P.R., Ouarda, T.B.M.J. and Ghedira, H. (2015) Urban climate modifications in hot desert cities: the role of land cover, local climate, and seasonality. *Geophysical Research Letters*, 42(22), 9980–9989. https://doi.org/10.1002/2015GL066534

Leaf, J.S. and Erell, E. (2017) A model of the ground surface temperature for micrometeorological analysis. *Theoretical and Applied Climatology*, 133, 1–14. https://doi.org/10.1007/s00704-017-2207-5

Liang, S. (2001) Narrowband to broadband conversions of land surface albedo I algorithms. *Remote Sensing Environment*, 76(2000), 213–238. https://doi.org/10.1016/S0034-4257(00)00205-4

Lookingbill, T.R. and Urban, D.L. (2003) Spatial estimation of air temperature differences for landscape-scale studies in montane environments. *Agricultural and Forest Meteorology*, 114(3–4), 141–151. https://doi.org/10.1016/S0168-1923(02)00196-X

Loridan, T. and Grimmond, C.S.B. (2012) Multi-site evaluation of an urban land-surface model: intra-urban heterogeneity, seasonality and parameter complexity requirements. *Quarterly Journal of the Royal Meteorological Society*, 138(665), 1094–1113. https://doi.org/10.1002/qj.963

Mandelmilch, M., Ben, N.O., Bäthge, A., Omer, I., Potchter, O. (2019) *Analysis of the Urban Heat Island magnitude in the Desert City of Beer-Sheva, Israel, Using a Modified Local Climate Zone Classification (Tromp Foundation Travel Award)*, Vol. 16.

Masson, V. (2000) A physically-based scheme for the urban energy budget in atmospheric models. *Boundary-layer meteorology*, 94 (3), 357–397.

Middel, A., Brazel, A.J., Gober, P., Myint, S.W., Chang, H. and Der, D.J. (2012) Land cover, climate, and the summer surface energy balance in Phoenix, AZ, and Portland, OR. *International Journal of Climatology*, 32(13), 2020–2032. https://doi.org/10.1002/joc.2408

Middel, A., Häb, K., Brazel, A.J., Martin, C.A. and Guhathakurta, S. (2014) Impact of urban form and design on mid-afternoon microclimate in Phoenix local climate zones. *Landscape and Urban Planning. Elsevier B.V.*, 122, 16–28. https://doi.org/10.1016/j.landurbplan.2013.11.004

Mills, G., Cleugh, H., Emmanuel, R., Endlicher, W., Erell, E., McGranahan, G., Ng, E., Nickson, A., Rosenthal, J. and Steemer, K. (2010) Climate information for improved planning and management of mega cities (needs perspective). *Procedia Environmental Sciences*, 1(1), 228–246. https://doi.org/10.1016/j.proenv.2010.09.015

Mirzaei, P.A. and Haghighat, F. (2010) Approaches to study urban heat island—abilities and limitations. *Building and Environment. Elsevier Ltd*, 45(10), 2192–2201. https://doi.org/10.1016/j.buildenv.2010.04.001

Moriasi, D.N., Arnold, J.G., Van Liew, M.W., Bingner, R.L., Harmel, R.D. and Veith, T.L. (2007) Model evaluation guidelines for systematic quantification of accuracy in watershed simulations. *Transactions of the ASABE*, 50(3), 885–900. https://doi.org/10.13031/2013.23153

Okabe, A., Boots, B., Sugihara, K. and Chiu, S.N. (2000) *Spatial Tessellations: Concepts and Applications of Voronoi Diagrams*. Hoboken, NJ: John Wiley & Sons, Inc..

Oke, T.R. (1981) Canyon geometry and the nocturnal urban heat island: comparison of scale model and field observations. *Journal of Climatology*, 1(3), 237–254. https://doi.org/10.1002/joc.3370010304

Oke, T.R. (1982) The energetic basis of the urban heat island. *Quarterly Journal of the Royal Meteorological Society*, 108(455), 1–24. https://doi.org/10.1002/qj.49710845502

Oke, T.R. (1987) *Boundary Layer Climates*. London: Methuen.

Oke, T.R., Grimmond, S., Spronken-Smith, R. (1998) On the confounding role of rural wetness in assessing urban effects on climate. In: *Second Urban Environment Symposium*, pp. 59–62.

OpenStreetMap contributors. (2017) *Planet dump*. Available at: https://planet.osm.org

Oyler, J.W., Ballantyne, A., Jencso, K., Sweet, M. and Running, S.W. (2015) Creating a topoclimatic daily air temperature dataset for the conterminous United States using homogenized station data and remotely sensed land skin temperature. *International Journal of Climatology*, 35(9), 2258–2279. https://doi.org/10.1002/joc.4127

Pearlmutter, D., Berliner, P. and Shaviv, E. (2007) Urban climatology in arid regions: current research in the Negev desert. *International Journal of Climatology*, 27(14), 1875–1885. https://doi.org/10.1002/joc.1523

Pebesma, E. (2018) Simple features for R: standardized support for spatial vector data. *The R Journal*, 10(1), 439–446. https://doi.org/10.32614/RJ-2018-009

Pelta, R., Chudnovsky, A.A. and Schwartz, J. (2016) Spatio-temporal behavior of brightness temperature in Tel-Aviv and its application to air temperature monitoring. *Environmental Pollution. Elsevier Ltd*, 208, 153–160. https://doi.org/10.1016/j.envpol.2015.09.007

Peng, S., Piao, S., Ciais, P., Friedlingstein, P., Ottle, C., Bréon, F.M., Nan, H., Zhou, L. and Myneni, R.B. (2012) Surface urban heat island across 419 global big cities. *Environmental Science and Technology*, 46(2), 696–703. https://doi.org/10.1021/es2030438

Pielke, R.A. (2001) Influence of the spatial distribution of vegetation and soils on the prediction of cumulus convective rainfall. *Reviews of Geophysics*, 39(2), 151–177. https://doi.org/10.1029/1999RG000072

Prihodko, L. and Goward, S.S.N. (1997) Estimation of air temperature from remotely sensed surface observations. *Remote Sensing of Environment*, 4257(96), 335–346. https://doi.org/10.1016/S0034-4257(96)00216-7

Qin, Z., Berliner, P.R. and Karnieli, A. (2005) Ground temperature measurement and emissivity determination to understand the thermal anomaly and its significance on the development of an arid environmental ecosystem in the sand dunes across the Israel–Egypt border. *Journal of Arid Environments*, 60(1), 27–52. https://doi.org/10.1016/j.jaridenv.2004.03.017

R Core Team R. (2014) *R: A Language and Environment for Statistical Computing*. Vienna, Austria: R Foundation for Statistical Computing.

Rosenfeld, A., Dorman, M., Schwartz, J., Novack, V., Just, A.C. and Kloog, I. (2017) Estimating daily minimum, maximum, and mean near surface air temperature using hybrid satellite models across Israel. *Environmental Research. Elsevier Inc.*, 159 (March), 297–312. https://doi.org/10.1016/j.envres.2017.08.017

Roth, M. (2007) Review of urban climate research in (sub)tropical regions. *International Journal of Climatology*, 27(14), 1859–1873. https://doi.org/10.1002/joc.1591

Runnalls, K.E. and Oke, T.R. (2000) Dynamics and controls of the near-surface heat island of Vancouver, British Columbia. *Physical Geography*, 21(4), 283–304. https://doi.org/10.1080/02723646.2000.10642711

Saaroni, H. and Ziv, B. (2010) Estimating the urban heat island contribution to urban and rural air temperature differences over complex terrain: application to an arid city. *Journal of Applied Meteorology and Climatology*, 49(10), 2159–2166. https://doi.org/10.1175/2010JAMC2473.1

Sailor, D.J. and Lu, L. (2004) A top–down methodology for developing diurnal and seasonal anthropogenic heating profiles for urban areas. *Atmospheric Environment*, 38(17), 2737–2748. https://doi.org/10.1016/j.atmosenv.2004.01.034

Sailor, D.J., Georgescu, M., Milne, J.M. and Hart, M.A. (2015) Development of a national anthropogenic heating database with an extrapolation for international cities. *Atmospheric Environment. Elsevier Ltd*, 118(2015), 7–18. https://doi.org/10.1016/j.atmosenv.2015.07.016

Salamanca, F., Georgescu, M., Mahalov, A., Moustaoui, M. and Wang, M. (2014) Anthropogenic heating of the urban environment due to air conditioning. *Journal of Geophysical Research: Atmospheres*, 119(10), 5949–5965. https://doi.org/10.1002/2013JD021225

Shastri, H., Barik, B., Ghosh, S., Venkataraman, C. and Sadavarte, P. (2017) Flip flop of day-night and summer-winter surface urban heat island intensity in India. *Scientific Reports. Nature Publishing Group*, 7(April 2016), 1–8. https://doi.org/10.1038/srep40178

Sheng, L., Tang, X., You, H., Gu, Q. and Hu, H. (2017) Comparison of the urban heat island intensity quantified by using air temperature and Landsat land surface temperature in Hangzhou, China. *Ecological Indicators. Elsevier Ltd*, 72, 738–746. https://doi.org/10.1016/j.ecolind.2016.09.009

Stewart, I.D. and Oke, T.R. (2012) Local climate zones for urban temperature studies. *Bulletin of the American Meteorological Society*, 93(12), 1879–1900. https://doi.org/10.1175/BAMS-D-11-00019.1

Svoma, B.M. and Brazel, A. (2010) Urban effects on the diurnal temperature cycle in Phoenix, Arizona. *Climate Research*, 41(1), 21–29. https://doi.org/10.3354/cr00831

Szymanowski, M. and Kryza, M. (2012) Local regression models for spatial interpolation of urban heat island-an example from Wrocław, SW Poland. *Theoretical and Applied Climatology*, 108 (1–2), 53–71. https://doi.org/10.1007/s00704-011-0517-6

UN. (2015) *World Urbanization Prospects* 2014*: The 2014 Revision, (ST/ESA/SER.A/366)*.

USGS. (2016) *LANDSAT 8 (L8) DATA USERS HANDBOOK version 2.0*.

Voogt, J. and Oke, T.R. (2003) Thermal remote sensing of urban climates. *Remote Sensing of Environment*, 86(3), 370–384. https://doi.org/10.1016/S0034-4257(03)00079-8

Weaver, C.P. and Avissar, R. (2001) Atmospheric disturbances caused by human modification of the landscape. *Bulletin of the American Meteorological Society*, 82(2), 269–281. https://doi.org/10.1175/1520-0477(2001)082<0269:ADCBHM>2.3.CO;2

Weng, Q., Lu, D. and Schubring, J. (2004) Estimation of land surface temperature—vegetation abundance relationship for urban heat island studies. *Remote Sensing of Environment*, 89(4), 467–483. https://doi.org/10.1016/j.rse.2003.11.005

Willmott, C.J. (1981) On the validation of models. *Physical Geography*, 2, 184–194. https://doi.org/10.1080/02723646.1981.10642213

Willmott, C.J. (1982) Some comments on the evaluation of model performance. *Bulletin of the American Meteorological Society*, 63 (11), 1309–1313. https://doi.org/10.1175/1520-0477(1982)063<1309:SCOTEO>2.0.CO;2

Willmott, C.J., Ackleson, S.G., Davis, R.E., Feddema, J.J., Klink, K. M., Legates, D.R., O'Donnell, J. and Rowe, C.M. (1985) Statistics for the evaluation and comparison of models. *Journal of Geophysical Research*, 90(C5), 8995. https://doi.org/10.1029/JC090iC05p08995

Williamson, T.J. (1995) *A confirmation technique for thermal performance simulation models. Building Simulation '95*. Madison, WI: IBPSA.

Yang, Y., Endreny, T.A. and Nowak, D.J. (2013) A physically based analytical spatial air temperature and humidity model. *Journal of Geophysical Research Atmospheres*, 118(18), 10449–10463. https://doi.org/10.1002/jgrd.50803

Yu, X., Guo, X. and Wu, Z. (2014) Land surface temperature retrieval from Landsat 8 TIRS—comparison between radiative transfer equation-based method, split window algorithm and single channel method. *Remote Sensing*, 6, 9829–9852. https://doi.org/10.3390/rs6109829

Zhao, L., Lee, X., Smith, R.B. and Oleson, K. (2014) Strong contributions of local background climate to urban heat islands. *Nature*, 511(7508), 216–219. https://doi.org/10.1038/nature13462

Zhou, B., Rybski, D. and Kropp, J.P. (2013) On the statistics of urban heat island intensity. *Geophysical Research Letters*, 40 (20), 5486–5491. https://doi.org/10.1002/2013GL057320

Zhu, W., Lű, A. and Jia, S. (2013) Estimation of daily maximum and minimum air temperature using MODIS land surface temperature products. *Remote Sensing of Environment. Elsevier Inc.*, 130, 62–73. https://doi.org/10.1016/j.rse.2012.10.034

SUPPORTING INFORMATION

Additional supporting information may be found online in the Supporting Information section at the end of this article.

How to cite this article: Zhou B, Kaplan S, Peeters A, Kloog I, Erell E. "Surface," "satellite" or "simulation": Mapping intra-urban microclimate variability in a desert city. *Int J Climatol*. 2020;40: 3099–3117. https://doi.org/10.1002/joc.6385